Electronic Supplementary Material (ESI) for Nanoscale Advances.
This journal is © The Royal Society of Chemistry 2024

Electronic Supplementary Information

Helical interfacial modulation for perovskite photovoltaics

Ghewa AlSabeh,[1,2#] Masaud Almalki,[1#] Sitthichok Kasemthaveechok,[3#] Marco A. Ruiz-Preciado,[1] Hong Zhang,[1‖] Nicolas Vanthuyne,[4] Paul Zimmermann,[5] Daphne Dekker,[6] Felix Thomas Eickemeyer[1], Alexander Hinderhofer,[5] Frank Schreiber,[5] Shaik M. Zakeeruddin[1], Bruno Ehrler,[6] Jeanne Crassous,[3*] Jovana V. Milić[1,2*], Michael Grätzel[1*]

[1]Laboratory of Photonics and Interfaces, Institute of Chemical Sciences and Engineering, École Polytechnique Fédérale de Lausanne, 1015 Lausanne, Switzerland; [2]Adolphe Merkle Institute, University of Fribourg, 1700 Fribourg, Switzerland; [3]Univ Rennes, CNRS, ISCR - UMR 6226, 35000 Rennes, France; [4]Aix Marseille University, CNRS Centrale Marseille, iSm2, 13284 Marseille, France [5]; Institut für Angewandte Physik, Universität Tübingen, 72076 Tübingen, Germany;[6] Center for Nanophotonics, AMOLF, Science Park 104, 1098 XG Amsterdam, the Netherlands. ‖Present address: State Key Laboratory of Photovoltaic Science and Technology, Shanghai Frontiers Science Research Base of Intelligent Optoelectronics and Perception, Institute of Optoelectronics, Fudan University, Shanghai 200433, China.

# Authors contributed equally to this work.

*Correspondence: jeanne.crassous@univ-rennes1.fr, jovana.milic@unifr.ch; michael.graetzel@epfl.ch

Table of Contents

S1. Materials and Methods

S1.1. Molecular Synthesis

Compounds were prepared in accordance with the adaptation of a previously reported procedure.[1-2]

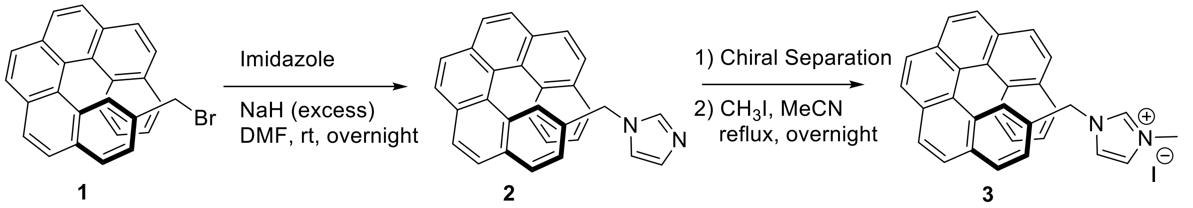

Scheme 1. Synthesis of the helicene systems **2** and **3** reported in this study.

2-(1-Methylene-imidazolyl)[6]helicene 2

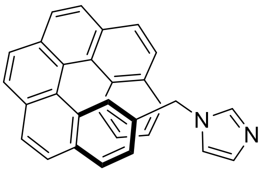

2

2-Bromomethylene[6]helicene **2**[1] (120 mg; 0.28 mmol; 1.0 eq) was mixed with a solution of sodium hydride (34 mg, 0.85 mmol, 3.0 eq) in *N*,*N*-dimethylformamide (10 mL) under argon atmosphere. Then, Imidazole (25 mg; 0.37 mmol, 1.3 eq) was added into the mixture. After stirring overnight, the mixture was poured into 50 mL of water and extracted with ethyl acetate (10 mL x 3). The organic layer was washed with brine and dried over $MgSO_4$. After removal of the solvent under reduced pressure, the crude product was purified by flash column chromatography with 5% Et_2O/heptane to 10% MeOH/EtOAc to obtain the desired product **2** as a beige solid (100 mg, quantitative). The two *P* and *M* enantiomers were obtained by chiral HPLC over a chiral stationary phase (*vide infra*).

^{1}H NMR (400 MHz, CD_2Cl_2) δ 7.97 – 8.06 (m, 7H), 7.93 (d, J = 8.6 Hz, 1H), 7.90 (dd, J = 8.0, 1.3 Hz, 1H), 7.82 (d, J = 8.2 Hz, 1H), 7.57 (dd, J = 8.6, 1.0 Hz, 1H), 7.44 – 7.50 (m, 1H), 7.32 (ddd, J = 8.0, 6.9, 1.2 Hz, 1H), 7.05 (s, 1H), 6.95 (dd, J = 8.2, 1.8 Hz, 1H), 6.87 (s, 1H), 6.71 (ddd, J = 8.4, 6.9, 1.4 Hz, 1H), 6.31 (s, 1H), 4.53 (d, J = 15.0 Hz, 1H), 4.36 (d, J = 15.1 Hz, 1H).

^{13}C NMR (101 MHz, $CDCl_3$) δ 137.1 (CH), 133.2 (C), 132.8 (C), 132.0 (C), 131.6 (C), 131.5 (C), 131.4 (C), 129.8 (C), 129.7 (C), 128.9 (CH_2), 128.5 (CH), 128.0 (CH), 127.7 (CH), 127.6 (C), 127.6 (C), 127.4 (CH), 127.4 (CH), 127.4 (CH), 127.3 (CH), 127.2 (CH), 127.0 (CH), 126.7 (CH x 2), 126.4 (CH), 125.8 (CH), 124.7 (CH), 124.3 (CH), 123.8 (C), 119.3 (CH), 50.4 (CH_2-N).

HR-MS Bruker MaXis 4G, ESI (+), CH_3OH/CH_2Cl_2: 90/10; ion $[M+H]^+$, $C_{30}H_{21}N_2$, m/z calculated 409.16992, m/z experimental 409.1701.

Experimental optical rotation values: ***P*-2**: $\left[\alpha_D^{25}\right]$=+2600, $\left[\phi_D^{25}\right]$ =+10950 (CH_2Cl_2 , 0.063 g·mL^{-1}); ***M*-2**: $\left[\alpha_D^{25}\right]$=+= -2600, $\left[\phi_D^{25}\right]$ = -10950 (CH_2Cl_2 , 0.038 g·mL^{-1}).

P **and** ***M*****-2-(1-Methylene-3-methyl-imidazolium)[6]helicene iodide salt 3**

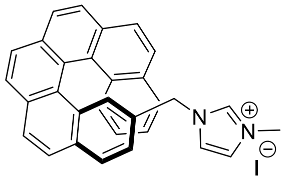

3

Methyl iodide (100 mL; 1.61 mmol) was mixed with *P*-2-(1-methylene-imidazolyl)[6]helicene **2** (15 mg; 0.04 mmol) in acetonitrile (3 mL). The mixture was refluxed overnight. After removal of acetonitrile under reduced pressure, the solid was washed with ethyl acetate and diethyl ether to afford the desired compound *P*-**3** as a yellow solid (15 mg; 75%). The same procedure was used for *M*-**2** to prepare *M*-**3**.

^{1}H NMR (400 MHz, CD_2Cl_2) δ 9.61 (s, 1H), 8.05– 8.15 (m, 5H), 8.03 (d, J = 3.8 Hz, 2H), 8.01 (s, 1H), 7.97 (d, J = 8.9 Hz, 1H), 7.91– 7.95 (m, 1H), 7.62 (d, J = 8.8 Hz, 2H), 7.26 – 7.47 (m, 2H), 7.24 – 7.08 (m, 1H), 6.76 (ddd, J = 8.5, 6.9, 1.4 Hz, 1H), 6.22 (d, J = 1.8 Hz, 1H), 5.09 (d, J = 14.4 Hz, 1H), 4.66 (d, J = 14.4 Hz, 1H), 4.03 (s, 3H).

^{13}C NMR (101 MHz, CD_2Cl_2) δ 136.5 (CH), 133.4 (C), 132.1 (C), 131.8 (C), 131.7 (C), 131.7 (C), 129.8 (C), 129.7 (C), 129.4 (CH), 128.7 (C), 128.2 (CH), 127.9 (CH), 127.8 (CH), 127.6 (CH), 127.6 (CHx2), 127.5 (CH), 127.5 (CH), 127.5 (CH), 127.4 (CH), 127.2 (CH), 126.8 (CH), 125.8 (CH), 125.4 (CH), 125.0 (CH), 123.6 (C), 123.2 (CH), 121.6 (CH), 53.2 (CH), 36.9 (CH_3).

HR-MS Bruker MaXis 4G, ESI (+), CH_3OH/CH_2Cl_2 : 90/10; ion $[M]^+$, $C_{31}H_{23}N_2$, m/z calculated 423.18557, m/z experimental 423.1856 (□=0 ppm).

Experimental optical rotation values: ***P*-3**: $[\alpha]_D^{25}$ = +2950 (± 1 %), $[\phi]_D^{25}$= -16400 (CH_2Cl_2 , 1 x 10^{-3} g·mL^{-1}); ***M*-3**: $[\alpha]_D^{25}$= -3100 (± 1 %), $[\phi]_D^{25}$= -17300 (CH_2Cl_2 , 1 x 10^{-3} g·mL^{-1})

S1.2. Chiral HPLC

The sample is dissolved in dichloromethane, injected on the chiral column, and detected with an UV detector at 290 nm. The flow-rate is 1 mL/min.

Table S1. Column characteristics

Column	Mobile Phase	t1	k1	t2	k2	α	Rs
Chiralpak IG	Heptane/ dichloromethane +triethylamine0.05% (30/70)	12.94	3.39	15.08	4.11	1.21	2.51

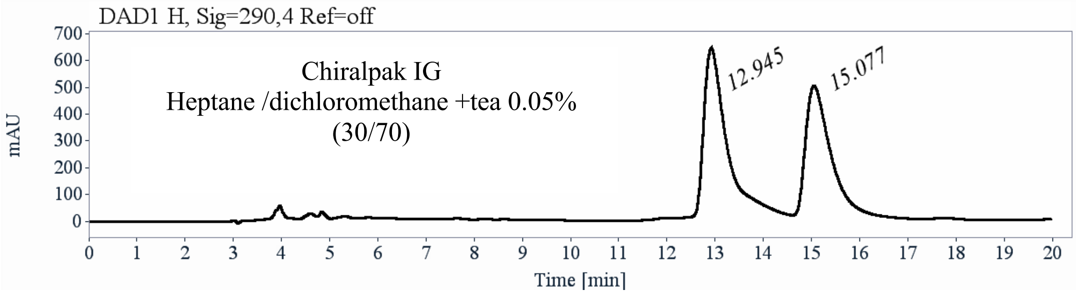

Figure S1. First purification chromatogram.

Table S2. First purification chromatogram characteristics.

RT [min]	Area	Area%	Capacity Factor	Enantioselectivity	Resolution (USP)
12.94	21854	53.85	3.39		
15.08	18727	46.15	4.11	1.21	2.51
Sum	40580	100.00			

Preparative separation for compound ***2****:*

- Sample preparation: About 60 mg of compound **2** are dissolved in 5 mL of dichloromethane.
- Chromatographic conditions: Chiralpak IG (250 x 4.6 mm), Hexane /dichloromethane+tea0.05% (30/70) as mobile phase, flow-rate = 5 mL/min, UV detection at 290 nm.
- Injections (stacked): 10 times 500 µL, every 18 minutes.

- *First fraction*: 18 mg of the first eluted with ee > 99.5 %

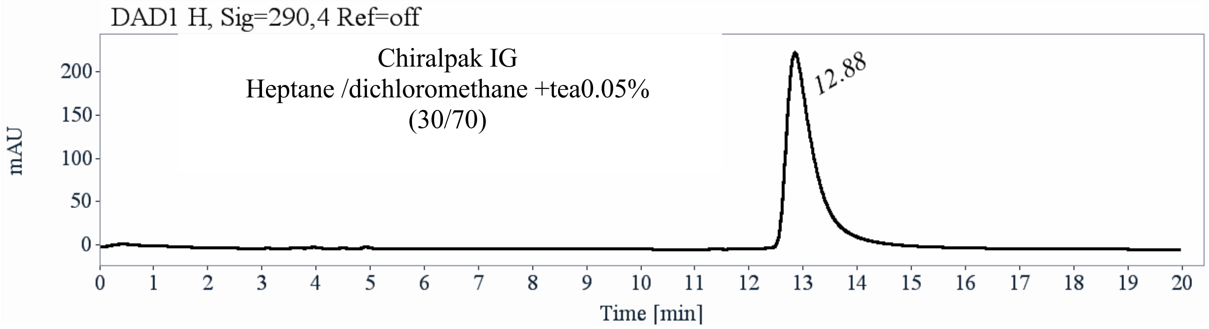

Figure S2. First fraction chromatogram.

Table S2. First fraction chromatogram characteristics.

RT [min]	Area	Area%
12.88	8601	100.00
Sum	8601	100.00

- *Second fraction-a:* 5.89 mg of the second eluted with ee > 99 %

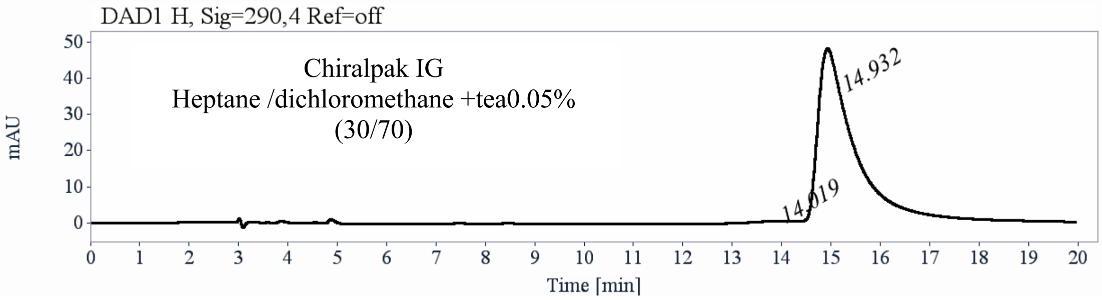

Figure S3. Second fraction-a chromatogram.

Table S3. Second fraction-a chromatogram characteristics.

RT [min]	Area	Area%
14.02	12	0.47
14.93	2568	99.53
Sum	2580	100.00

- *Second fraction-b:* 0.85 mg of the second eluted with ee > 97 %

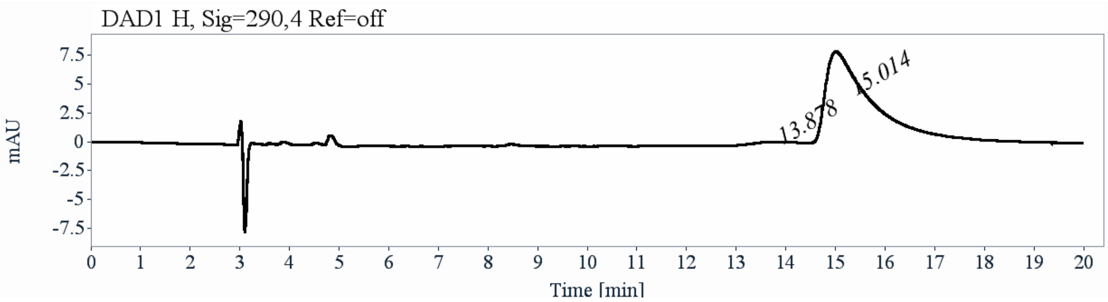

Figure S4. Second fraction-b chromatogram.

Table S4. Second fraction-b chromatogram characteristics.

RT [min]	Area	Area%
13.88	8	1.41
15.01	564	98.59
Sum	572	100.00

- *Second fraction-c:* 9.9 mg of the second eluted with ee > 98.5 %

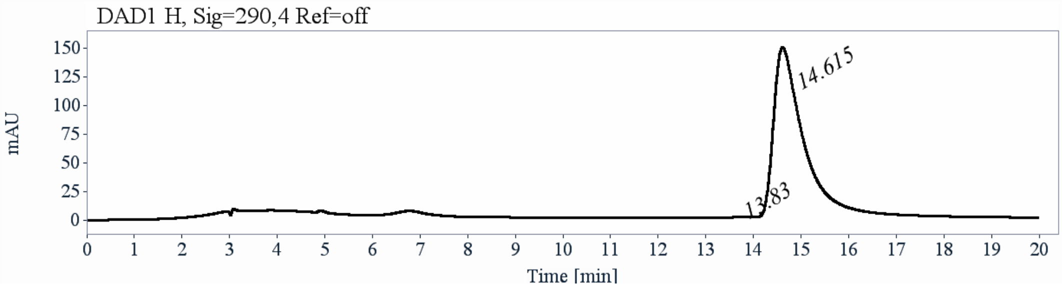

Figure S5. Second fraction-c chromatogram.

Table S5. Second fraction-c chromatogram characteristics.

RT [min]	Area	Area%
13.83	37	0.53
14.61	6867	99.47
Sum	6904	100.00

S1.2. Molecular Characterization

Thin-layer chromatography (TLC) was performed on aluminum sheets precoated with Merck 5735 Kieselgel 60F254. Column chromatography was carried out with Merck 5735 Kieselgel 60F (0.040-0.063 mm mesh). Chemicals were purchased from commercial source and used as received.

^{1}H and ^{13}C NMR spectra were recorded at room temperature on an *AVANCE III 400 BRUKER* or an *AVANCE I 400 BRUKER* at Centre Régional de Mesures Physiques de l'Ouest (CRMPO), Université de Rennes 1. Chemical shifts are given in ppm and coupling constants *J* in Hz. Chemical shifts for ^{1}H NMR spectra are referenced relative to residual protium in the deuterated solvent (5.32 ppm, CD_2Cl_2). ^{13}C shifts are referenced to CD_2Cl_2 peaks at 54.00 ppm.

High-resolution mass (HR-MS) determinations were performed at CRMPO on a Bruker MaXis 4G by ESI method. Experimental and calculated masses are given with consideration of the mass of the electron.

UV-Visible (UV-vis, in M^{-1} cm^{-1} (liquid state) and a.u. (solid state)) absorption spectra were recorded on Specord 205 UV-vis-NIR spectrophotometer using quartz cuvettes of 1 cm path length for liquid phase measurement and Jasco V-770 spectrophotometer for solid state measurement.

Electronic circular dichroism (ECD, in M^{-1} cm^{-1} (liquid state) and mdeg (solid state)) was measured on a Jasco J-815 Circular Dichroism Spectrometer (IFR140 facility - Biosit - Université de Rennes 1).

S1.3. Thin Film Fabrication

Commercial materials were used in the film preparation: titanium diisopropoxide bis(acetylacetonate) (75 wt% in isopropanol, Sigma-Aldrich); anhydrous ethanol (99.5%, Fischer Scientific); TiO_2 paste (Dyesol 30 NR-D); tin(IV) oxide colloidal dispersion (15% in water, Alfa Aesar); nickel nitrate hexahydrate (Ni(NO3)2·6H2O, 99.99%, Sigma Aldrich); 2- methoxyethanol (99%, Roth); [6,6]-Phenyl-C61-butyric acid methyl ester (PC60BM, Sigma Aldrich); chlorobenzene (99.8%, ACROS); bathocuproine (98%, TCI); Spiro-OMeTAD (99%); lithium bis(trifluoro-methylsulphonyl)imide (Li-TFSI, 99.95%, Sigma Aldrich); 4-*tert*-butylpyridine (4-tBP, 96%, Sigma-Aldrich); lead iodide (PbI2, 99.9985%, Alfa Aesar); formamidinium iodide (FAI, 398%, Greatcellsolar); methylammonium iodide (MAI, 398%, Greatcellsolar); methylammonium chloride (MACl, 99%, Dyenamo); dimethylformamide (DMF, 99.8%, Acros); dimethyl sulfoxide (DMSO, 99.7%, Acros).

Hybrid perovskite thin films were fabricated based on either $(FA_{0.97}MA_{0.03}Pb(I_{0.97}Br_{0.03})_3$ (*procedure 1*) or $FA_{0.9}MA_{0.1})_{0.95}Cs_{0.05}Pb_{1.03}(I_{0.93}Br_{0.1})_3$ (*procedure 2*) compositions by spin-coating the perovskite precursor solution on the substrates (specified in figure captions) through a stepwise preparation process reported previously.[3-4] The substrates were cleaned with oxygen plasma for 15 min before deposition. A comparable procedure was used for the devices, complemented by the deposition of the hole-transporting layer and Au electrodes. Although *procedure 2* yielded comparatively higher photovoltaic performance with comparable characteristics (Figures S15 and S24), *procedure 1* provided better reproducibility (Figures 3–4 and S25), and it was thus primarily used for thin-film and device characterization and stability measurements (Figures 2–4, S16–S23, S25–26), unless otherwise stated.

S1.4. Device Fabrication

Photovoltaic devices were fabricated using the *n-i-p* architecture with the constituent layers as follows: FTO/(40 nm) c-TiO_2/(250 nm) mp-TiO_2/(450 nm) perovskite/(180 nm) Spiro-OMeTAD/(80 nm) Au based on the reported procedure.[3] An active area of 0.25 cm^2 (5 mm × 5 mm) was defined by the gold electrodes, and a 0.16 cm^2 black metal mask was used during measurements to define the aperture area. For this purpose, glass sheets covered by fluorine-doped tin oxide (Nippon sheet glass 8 $\Omega \cdot sq^{-1}$) was thoroughly brushed with a 10% Hellmanex (Hellma GmbH) water solution and then placed under sonication in a 2% Hellmanex water solution for 30 min. After that, the Hellmanex solution was replaced by acetone and later ethanol and sonicated for 15 min and 10 min, respectively. Then, a ca. 40 nm-thick TiO_2 compact layer (c-TiO_2) was deposited by spray pyrolysis with a precursor solution of titanium diisopropoxide bis(acetylacetonate) (75 wt% in isopropanol, Sigma-Aldrich) in anhydrous ethanol (99.5%, Fischer Scientific) at 450 °C. After the spraying, the substrates were kept at 450 ºC for 30 min. Then, a suspension of TiO_2 paste (Dyesol 30 NR-D) in ethanol was used to cast a ca. 250 nm-thick mesoporous TiO_2 (mp-TiO_2) layer by spin coating at 4000 rpm for 20 s with an acceleration of 2000 rpm s^{-1}. After the spin coating, the solvent was allowed to evaporate on a hot plate at 80 °C for 10 min and then sintered at 450 °C for 30 min under dry air flow. UV-ozone treatment for 15 min was used before the deposition of the c-TiO_2 and mp-TiO_2 layers. A ca. 450 nm-thick perovskite layer was deposited by spin-coating following the antisolvent method based on either *procedure 1 or 2*.

Procedure 1: The perovskite layer was deposited using a single-step deposition method from a precursor solution based on $FA_{0.97}MA_{0.03}Pb(I_{0.97}Br_{0.03})_3$ composition. The solution was prepared in Ar atmosphere by dissolving PbI_2 (1.51 M), FAI (1.47 M), and MABr (0.03 M), $PbBr_2$ (0.03 M) and MACl (0.6 M) in anhydrous DMF / DMSO (4:1 (v:v)). The precursor solution was spin-coated onto the mp-TiO_2 films in a one-step program at 600 and 5000 rpm for 30 s. 200 μl of chlorobenzene was dropped on the spinning substrate 10 s prior to the end of the program. This was followed by annealing at 150 °C for 10 min. The substrates were cooled down to room temperature before depositing 100 μL of helicene solution in 1,1,2,2-tetrachloroethane (0.5–1 mg/mL) while substrates were spin-coated at 5000 rpm for 30 sec followed by heating at 100 °C for 5 min. HTM was deposited onto perovskite films by spin-coating at 4000 rpm for 20 s. HTL involved 90 mg of Spiro-OMeTAD doped with LiTFDI (17.8 μl prepared by dissolving 520 mg LiTFSI in 1 mL of acetonitrile) and 28.8 μl of 4-tBP dissolved in 1 mL of chlorobenzene. Finally, ~80 nm gold (Au) layer was thermally evaporated.

Procedure 2: The precursor solution based on $(FA_{0.9}MA_{0.1})_{0.95}Cs_{0.05}Pb_{1.03}(I_{0.93}Br_{0.1})_3$ composition was drop-casted on the substrates and spun at 2000 rpm (200 rpm s^{-1} acceleration) and 6000 rpm (acceleration of 2000 rpm s^{-1}) for 10 s and 30 s, respectively. During the last 10 s of the second spin-coating step, 220 μL of the α,α,α-trifluorotoluene antisolvent (TFT, 99%, anhydrous, Sigma-Aldrich) was drop-casted. The perovskite film was then dried on a hot plate at 100 °C for 60 min. The substrates were allowed to cool down for 10 min. A 60 μL of the solution of helicene of the concentration of 0.5–1 mg/mL dissolved in 1,1,2,2-tetrachloroethane was deposited, which was followed by spin-coating at 5000 rpm for 30 sec and heating at 80 °C for 10 min. A 70 mM solution of Spiro-OMeTAD (99%, Merck) in chlorobenzene (CB, 99.8%, ACROS) was prepared. Lithium bis(trifluoromethylsulphonyl)imide (Li-TFSI) and 4-*tert*-butylpyridine (4-tBP) were used as additives in a 0.5 and 3.3 mol% (relative to Spiro-OMeTAD), respectively. This solution was spin-coated on the perovskite film at 2000 rpm (acceleration of 1200 rpm s^{-1}) for 20 s to form a ca. 180 nm HTL in a dry air glovebox. In the final step, 80 nm gold electrodes were deposited by thermal evaporation to complete the device.

S1.5. Thin Film and Device Characterization

Attenuated total reflection Fourier Transform Infrared spectroscopy (ATR-FTIR) was measured with Nicolet 6700 (ThermoFisher Scientific) with ATR obtained with the golden gate accessory from Specac.

X-ray diffraction (XRD) patterns were recorded on an X'Pert MPD PRO (PANanalytical) equipped with a ceramic tube providing Ni-filtered (Cu anode, λ = 1.54060 Å) radiation and a RTMS X'Celerator (PANalytical). The measurements were done in BRAGG-BRENTANO geometry from 2θ = 5–60 °. The samples were mounted without further modification, and the automatic divergence slit (10 mm) and beam mask (10 mm) were adjusted to the dimension of the films.

Grazing Incidence Wide Angle X-ray Scattering (GIWAXS) was measured at the Soleil synchrotron. A XPAD140 detector was used. Beam energy was 18.420 keV, all scans were measured at an angle of incidence a_0 = 0.2, which is close to the critical angle and surface sensitive, and they were done in a nitrogen atmosphere.

UV-Vis absorption measurements were recorded using Varian Cary5 UV–visible spectrophotometer.

Steady-state photoluminescence (PL) spectra were recorded by exciting the layered perovskite films deposited onto microscope glass. The emission between was recorded with a Fluorolog 322 spectrometer (Horiba Jobin Yvon iHr320 and a CCD). The samples were mounted at 60° and emission recorded at 90° from the incident beam path. *Time-Resolved Photoluminescence* (TRPL) was measured via time-correlated single photon counting (TCSPC) using a LifeSpec II (Edinburgh Instruments) fluorescence spectrometer with a picosecond pulsed diode laser (EPL-510, Edinburgh Instruments) at 510 nm wavelength and 85 ps pulse width. *Photoluminescence quantum yield* (PLQY) was measured using an integrating sphere (Fluorolog, Horiba JobinYvon), an Andor Kymera 193i spectrograph, and a 660 nm continuous-wave laser (OBIS, Coherent) set at 1-Sun equivalent photon flux (1.1 µm beam full-width half-maximum, 632 µW); photoluminescence was collected at normal incidence using a 0.1 NA, 110 µm-diameter optical fiber.[5] For the absolute spectral calibration of the PLQY measurement system, we used a radiometrically calibrated halogen lamp (HL-3 plus CAL from Ocean Optics).

Steady-state photoluminescence (PL) spectra at different magnetic field strengths were recorded by placing modulated films based on $FA_{0.97}MA_{0.03}Pb(I_{0.97}Br_{0.03})_3$ compositions on microscopic glass between the poles of a GMW 3470 45 mm electromagnet in an airtight sample holder, leaving a distance of 4 cm between the poles. The films were excited using a 405 nm ThorLabs S1FC405 laser, and the PL was collected using an Ocean Optics USB4000 detector. The magnetic field strength was set by controlling the current through the electromagnet (shown in Figures S21–S23).

Current-voltage characteristics were obtained under standard AM 1.5G illumination at a light intensity of 100 mW cm^{-2}. The *J-V* curves are recorded at a scanning rate of 50 mV s^{-1} under standard AM 1.5G solar radiation and reverse bias (from V_{OC} to J_{SC}). *stability measurements* were performed using Fluxim Litos Lite system by monitoring maximum power point under N_2 atmosphere at ambient temperature.

Contact angles were measured with a drop shape analyzer (KRÜSS, DSA100) at ambient temperature.

S2. Supplementary Data

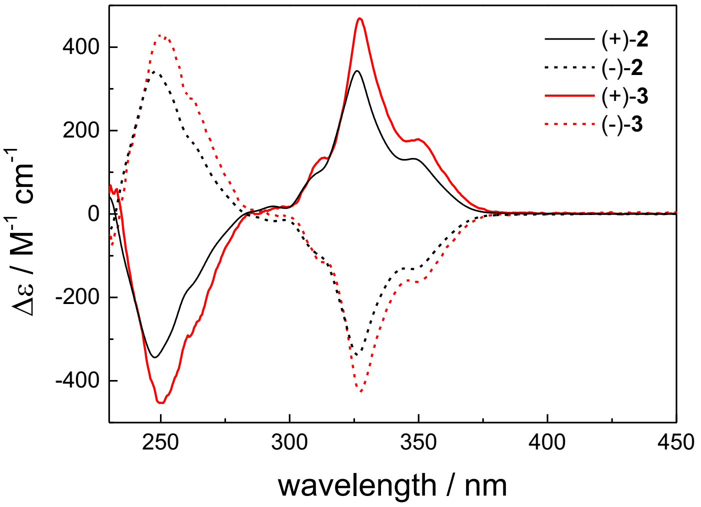

Figure S6. CD spectra of the enantiopure of (+)- **2** (black, solid line) and **3** (red, solid line), and corresponding (-) enantiomer are in dash line (C ~ 1×10^{-5} M).

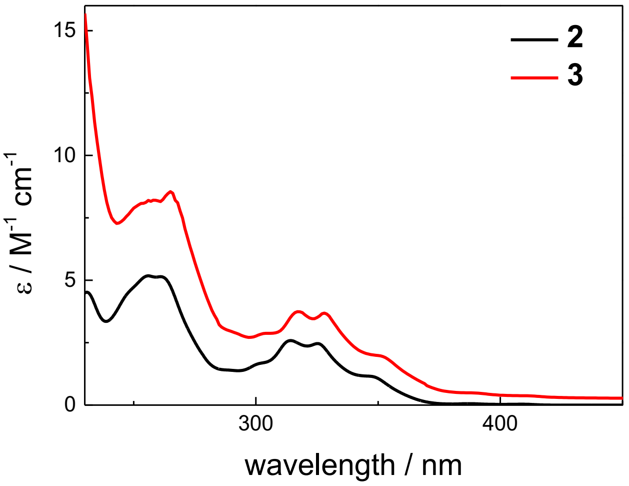

Figure S7. UV-vis spectra of compounds **2** and **3** in CH_2Cl_2 (C ~ 1×10^{-5} M).

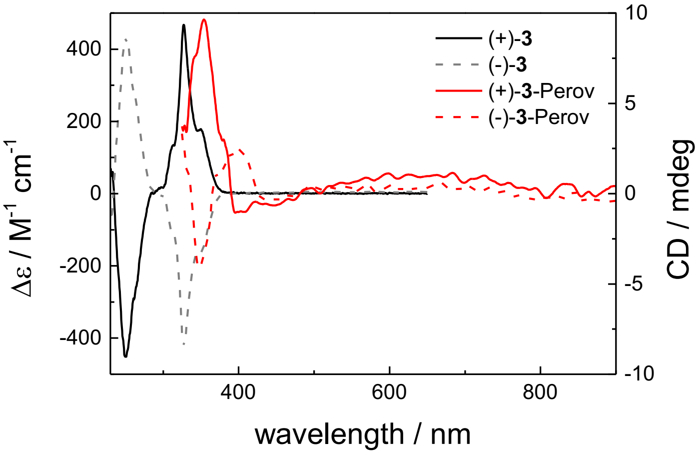

Figure S8. ECD spectra of compound (+)-**3** in CH_2Cl_2 (C ~ 1×10^{-5} M, black solid line) and (+)-**3** on perovskite system (red solid line). Corresponding (-) enantiomer are shown in dash line.

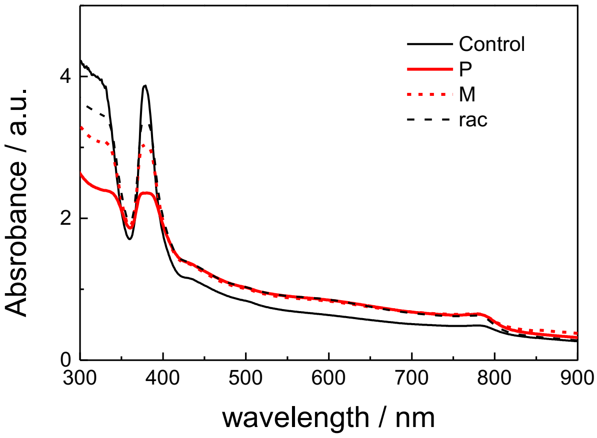

Figure S9. UV-vis-NIR spectra of perovskite on glass plate containing (+)-**3** (solid red line), (-)-**3**, (dash red line), *rac*-**3** (dash black line), control (solid black line).

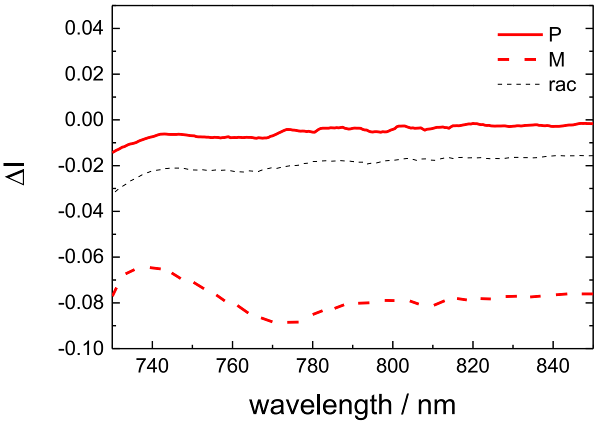

Figure S10. CPL spectra of perovskite on glass plate containing (+)-**3** (solid red line), (-)-**3**, (dash red line), *rac*-**3** (dash black line).

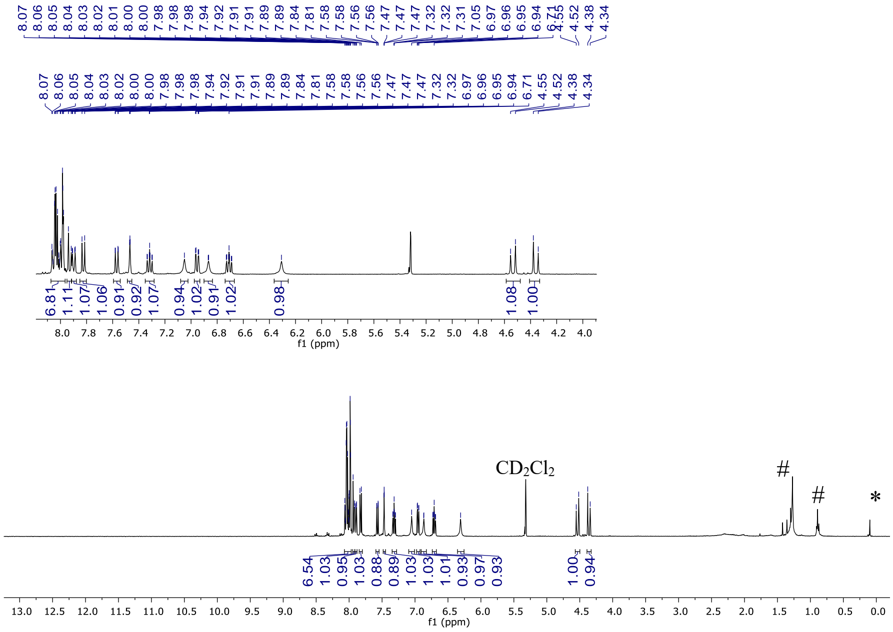

Figure S11. ^{1}H-NMR spectrum (400 MHz, CD_2Cl_2) of compound **2**. # denotes trace of heptane, * denotes traces of grease.

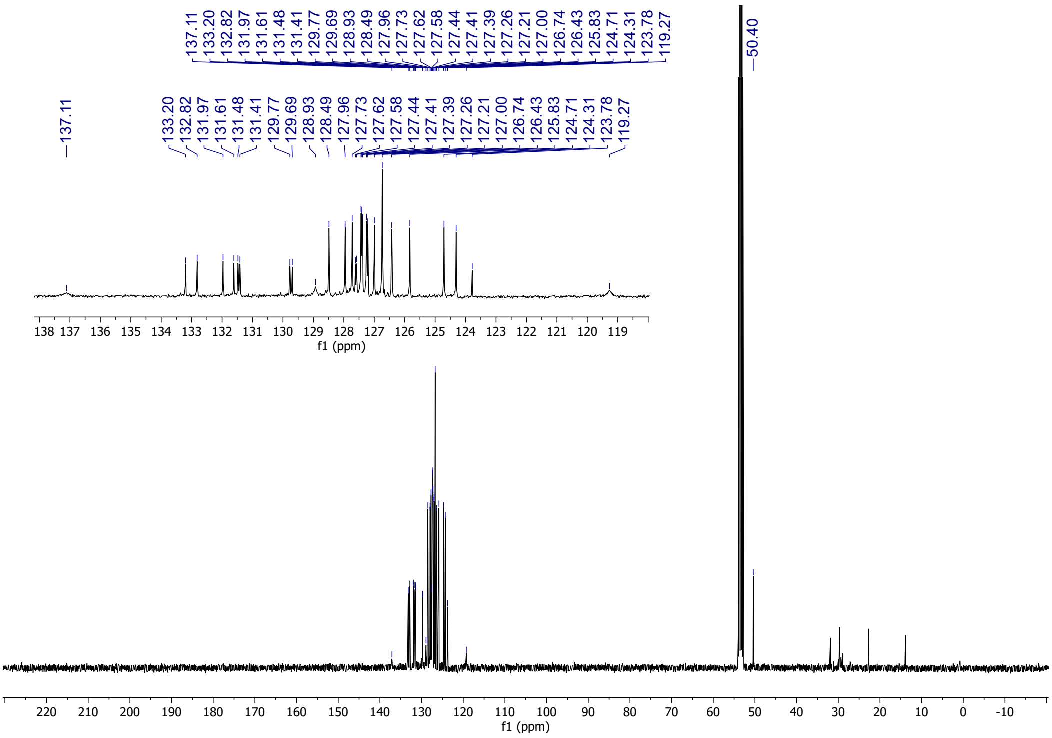

Figure S12. ^{13}C-NMR spectrum (100 MHz, CD_2Cl_2) of compound **2**. # denotes traces of heptane. * denotes traces of grease.

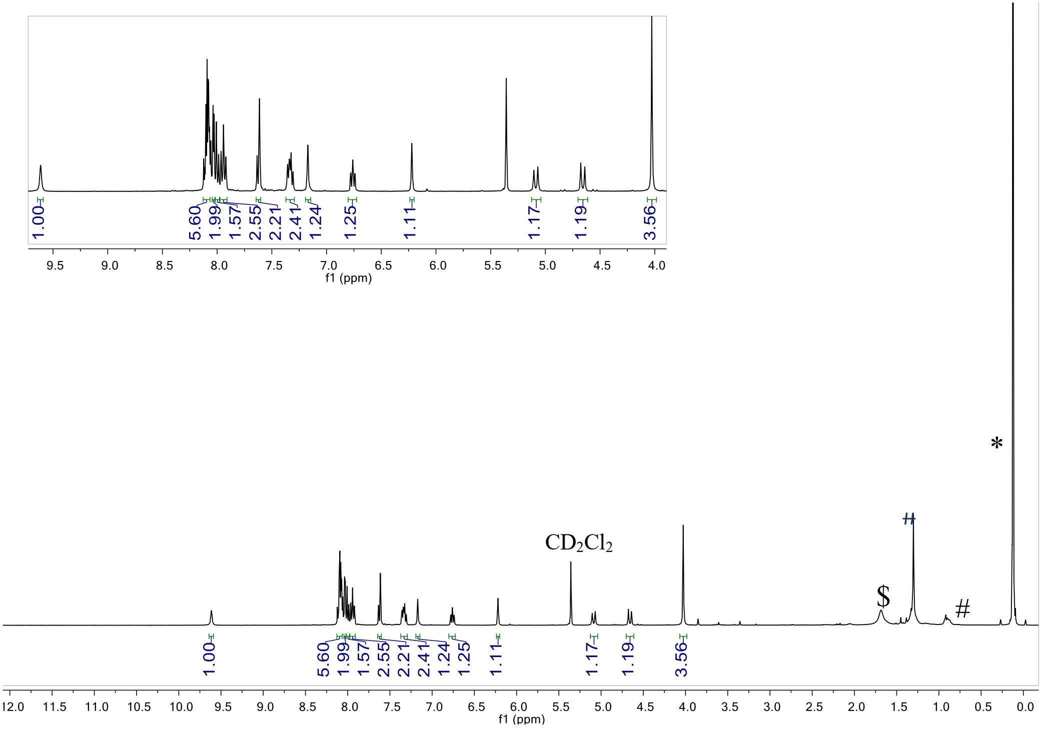

Figure S13. ^{1}H-NMR spectrum (400 MHz, CD_2Cl_2) of compound **3**. * denotes traces of grease, $ denotes traces of water, # denotes traces of solvent.

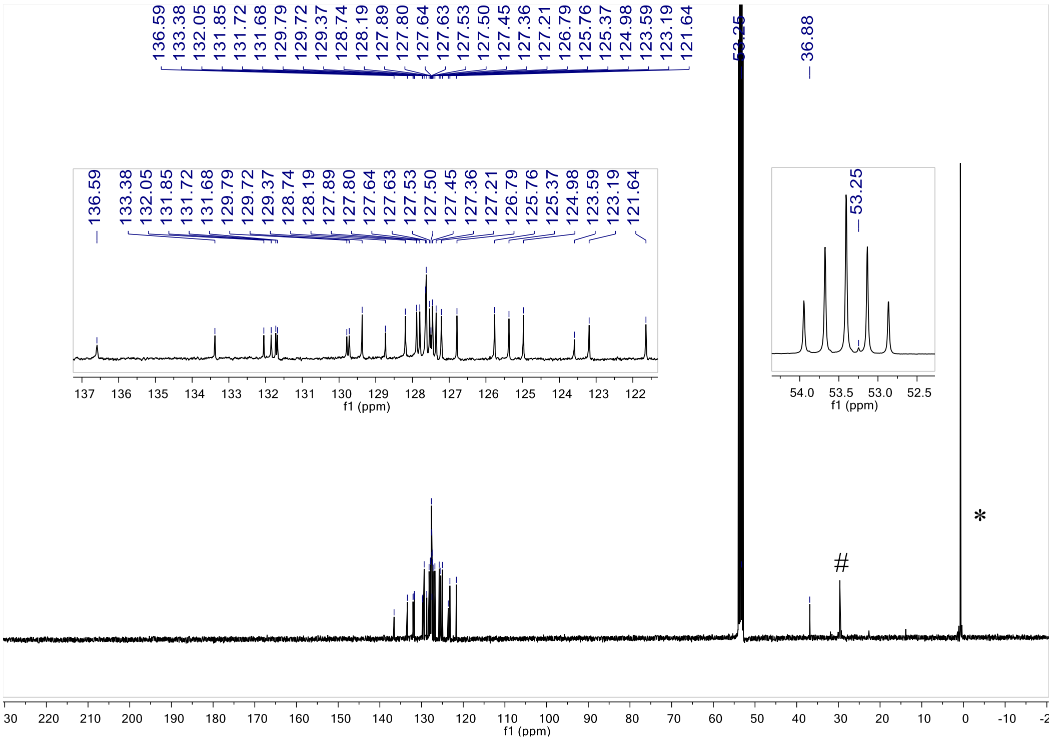

Figure S14. ^{13}C-NMR spectrum (101 MHz, CD_2Cl_2) of compound **3**. *denotes traces of silicon grease, # denotes traces of grease.

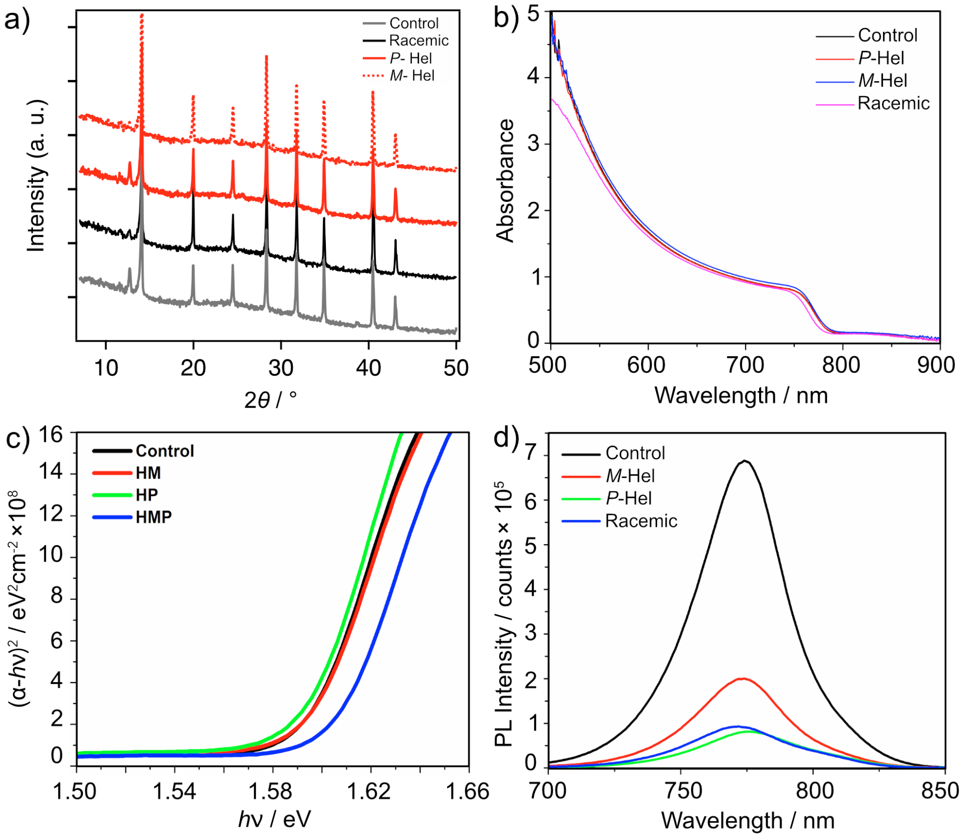

Figure S15. Effect of helical modulation on the properties of perovskite films. (a) XRD patterns, (b) UV-vis absorption spectra with the (c) corresponding Tauc plots and (d) PL emission spectra of control (black) and modulated films based on $(FA_{0.9}MA_{0.1})_{0.95}Cs_{0.05}Pb_{1.03}I_3$ compositions (*procedure 2*) on microscope glass. The racemic mix (HMP) here is based on Cl ions, unlike I-based enantiomers.

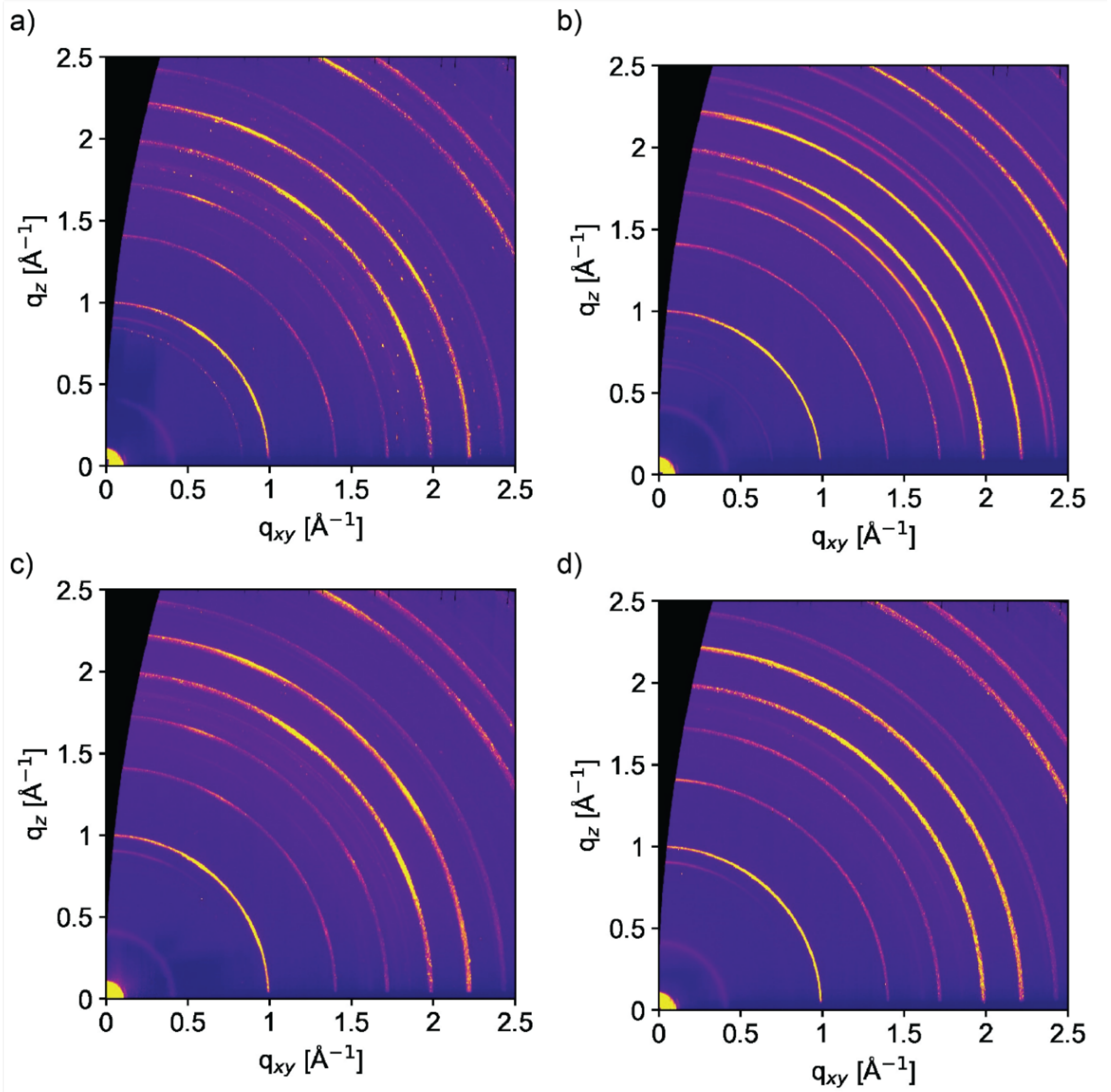

Figure S16. Grazing incidence wide-angle x-ray scattering (GIWAXS) images of control (a) and modulated films based on $(FA_{0.9}MA_{0.1})_{0.95}Cs_{0.05}Pb_{1.03}(I_{0.93}Br_{0.1})_3$ composition incorporating *P*-Hel (b), *M*-Hel (c), and racemic (d) compounds on FTO glass substrates.

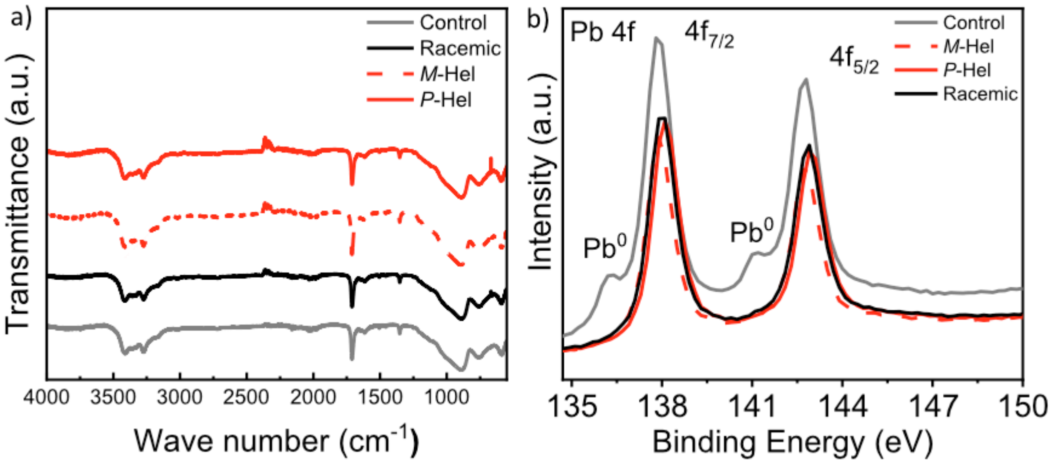

Figure S17. (a) FTIR and (b) XPS spectra of control and modulated (*M*, *P*, *racemic*) films based on $FA_{0.97}MA_{0.03}Pb(I_{0.97}Br_{0.03})_3$ composition.

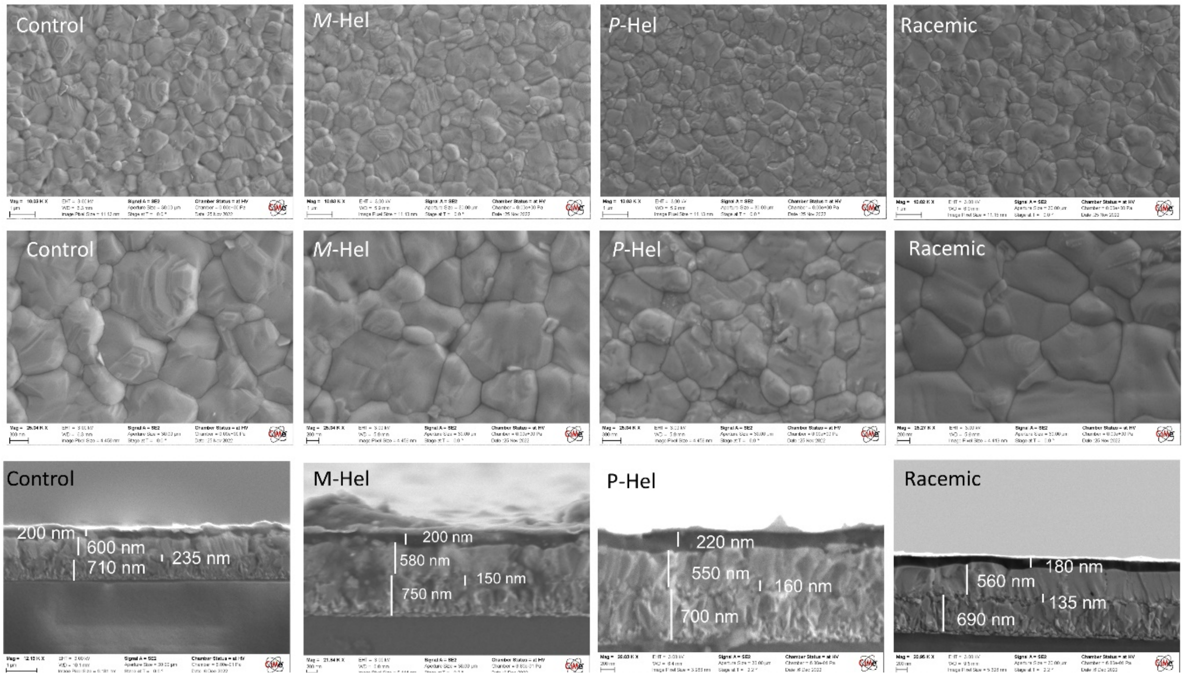

Figure S18. SEM images of film surface (top) and cross-section (bottom) on FTO glass. The thicknesses correspond to the FTO, TiO_2, 3D perovskites and the spiro-OMeTAD layers. The modulation layers are less than 10 nm in thickness, and the gold layer is around 80 nm thickness.

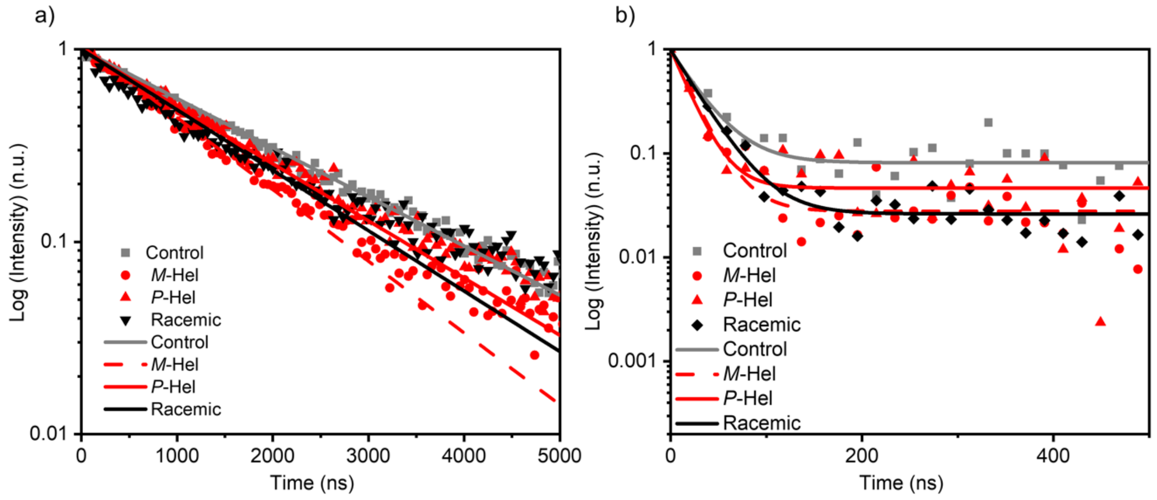

Figure S19. Time-resolved PL measurements of $FA_{0.97}MA_{0.03}Pb(I_{0.97}Br_{0.03})_3$ thin films on glass (a) without and (b) with Spiro-OMeTAD.

Table S6. PL quantum yields of the $FA_{0.97}MA_{0.03}Pb(I_{0.97}Br_{0.03})_3$ perovskites on microscope glass in the absence (Figure 2c) and presence (Figure 2d) of hole-transport material (Spiro-OMeTAD), and the calculated quasi-Fermi level splitting (QFLS) (ΔE_F) values.

	Control	*M*-Hel	*P*-Hel	Racemic
PLQY (without Spiro-OMeTAD) (%)	18.2	20.5	25.2	29.0
PLQY (with Spiro-OMeTAD) (%)	0.53	0.20	0.15	0.91
QFLS (with Spiro-OMeTAD) (ΔE_F) (V)	1.14	1.12	1.11	1.15

Table S7. PL intensity decay lifetime (based on data shown in Figure S19)

	t_1 (ns)
Without Spiro-OMeTAD	
Control	1700.20 ± 6.03
M-Hel	1164.42 ± 6.88
P-Hel	1461.87 ± 7.17
Racemic	1382.80 ± 14.45
With Spiro-OMeTAD	
Control	29.02 ± 3.07
M-Hel	21.81 ± 0.00
P-Hel	19.46 ± 1.48
Racemic	28.67 ± 0.93

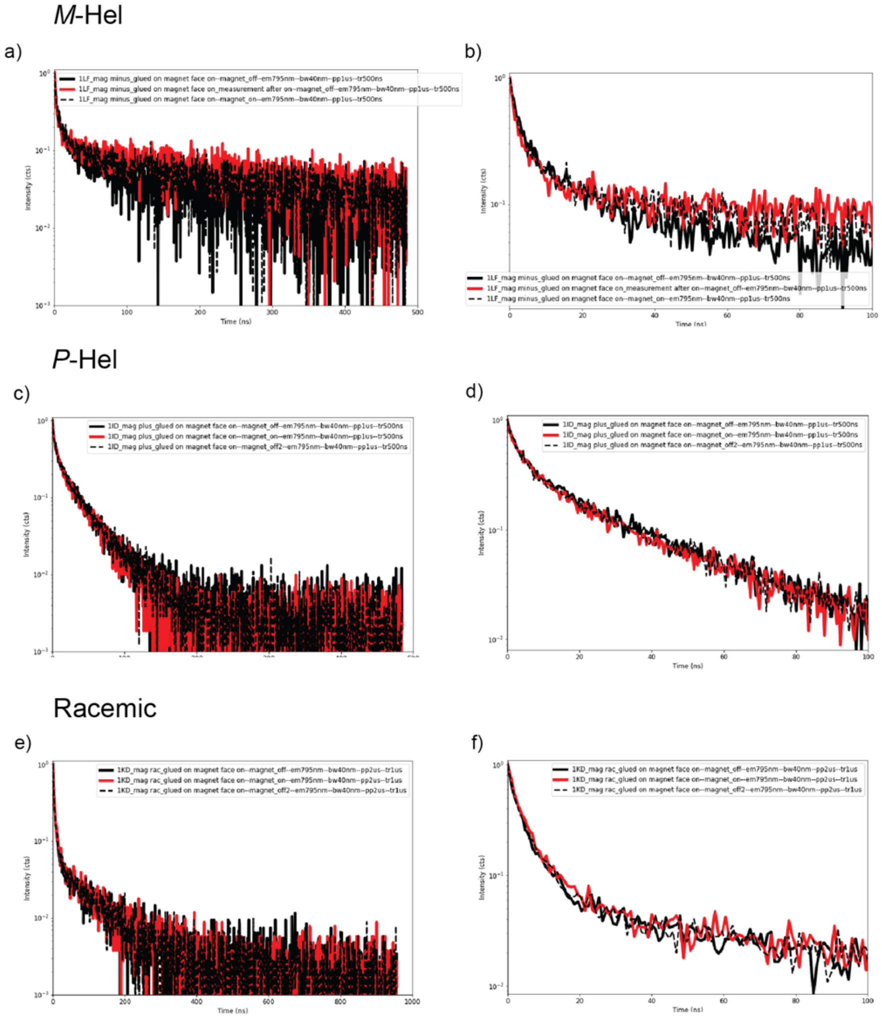

Figure S20. Time-resolved PL measurements of $FA_{0.97}MA_{0.03}Pb(I_{0.97}Br_{0.03})_3$ thin films on glass before and after exposure to the magnetic field, indicating no substantial changes under these conditions. In case of significant CISS effect, we would expect higher charge transfer for the modulated samples in the presence of magnetic field, resulting in different charge transfer kinetics, which was not the case.

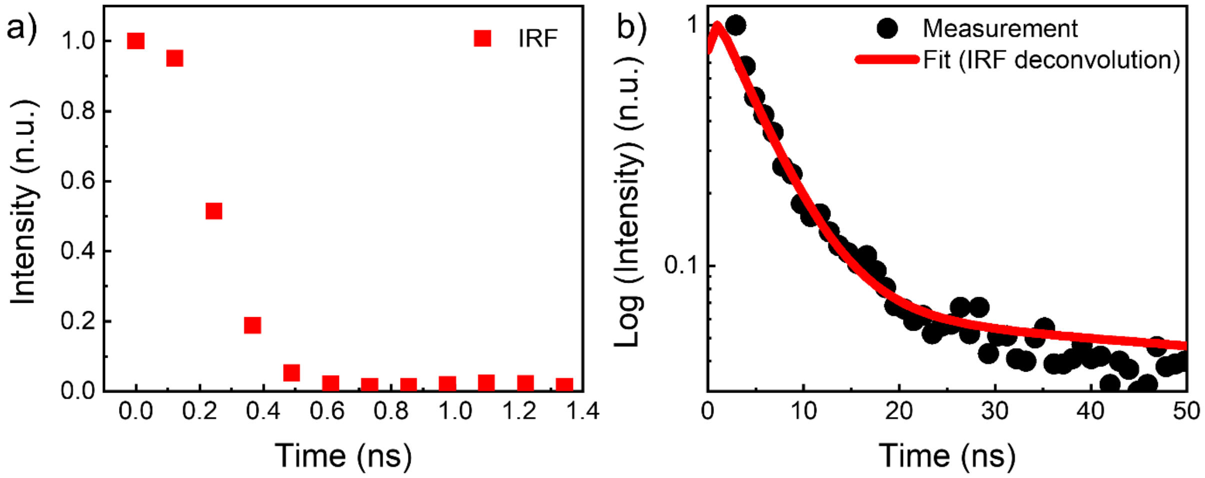

Figure S21. (a) Instrument response function (IRF) and (b) measurement and deconvolution fit of the time-resolved PL decay of the fastest decay measured in this work (racemic mixture, Figure S20). The decay time of IRF is around 300 ps, which is significantly shorter than the fastest decay time in our work (7 ns). The deconvolution fit shows no difference with the measured data (b), which is expected since IRF is much shorter. Since all TRPL decay times are longer, the lifetimes obtained from a non-deconvolution fit are the same as those obtained with deconvolution.

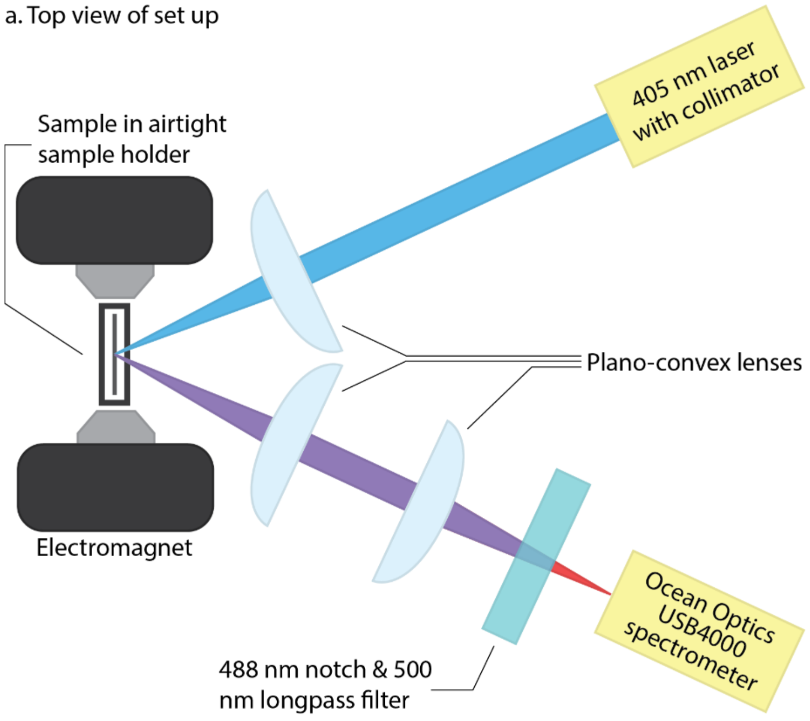

b. Currents and corresponding magnetic field strenghts

Current (A)	**Magnetic field (mT)**
0	0
0.5	20
1	40
2	90
3	130
4	180
5	220
6	260
7	290
8	320
9	340

Figure S22. (a) Schematic overview of the top view of the set up used to measure steady-state PL spectra under the influence of a magnetic field. (b) The currents used during the PL measurements and the corresponding magnetic field strengths. Further details are provided in Figures S23–S24 (Section S3).

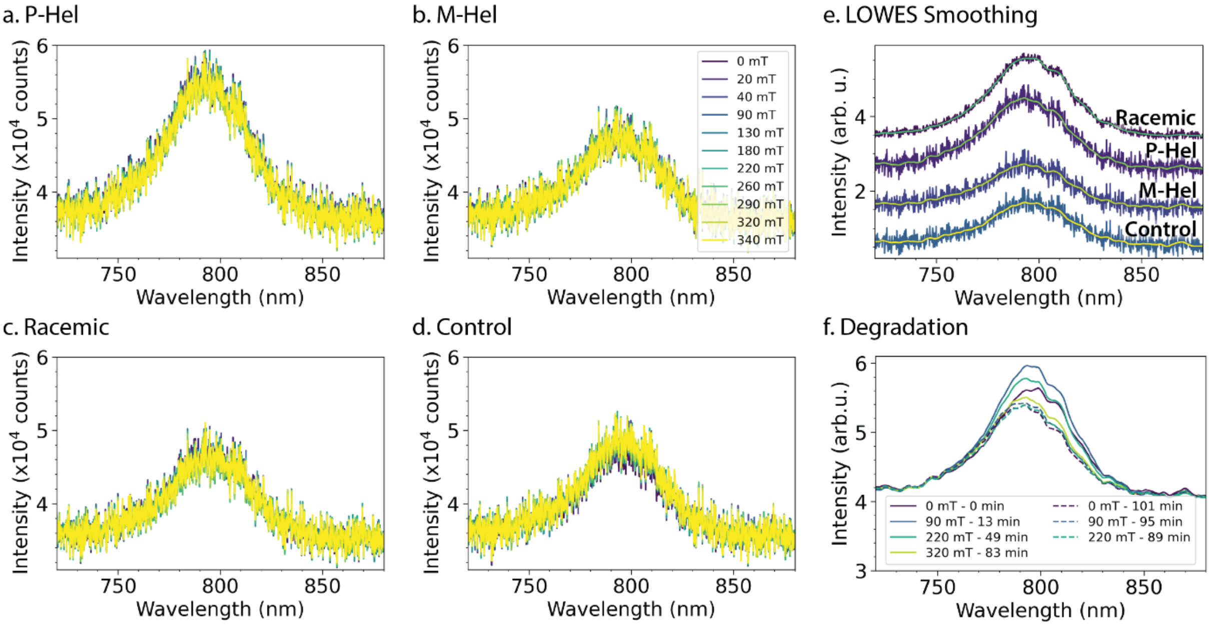

Figure S23. (a-d) PL spectra recorded at a range of magnetic field strengths. All spectra were recorded using an excitation laser power of 0.3 mW and an integration time of 600 ms, except the spectra of the control (d), which were recorded using 0.55 mW. (e) Smoothed PL spectra superimposed on the corresponding raw PL spectra at 0 mT. (f) PL spectra of the *M*-Hel sample recorded at different magnetic field strengths, and the PL spectra recorded at the same magnetic field strengths at a later time point. The timestamps are relative to the first measurement at 0 mT.

a. P-Hel

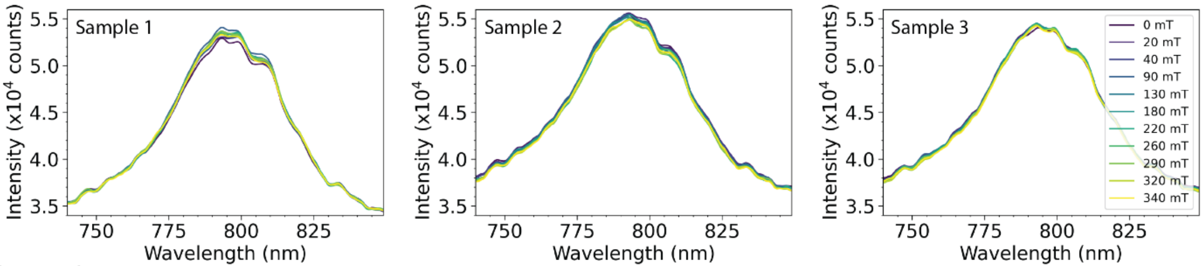

b. M-Hel

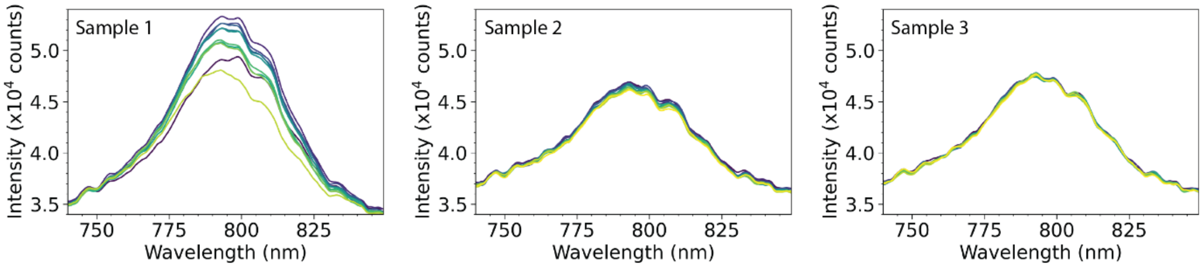

c. Racemic

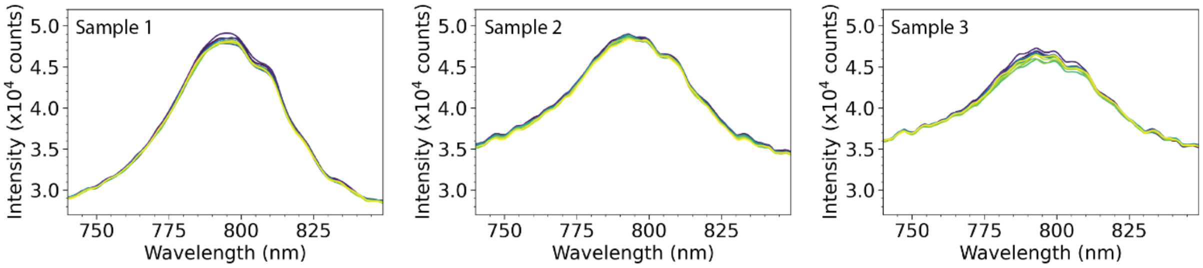

d. Control

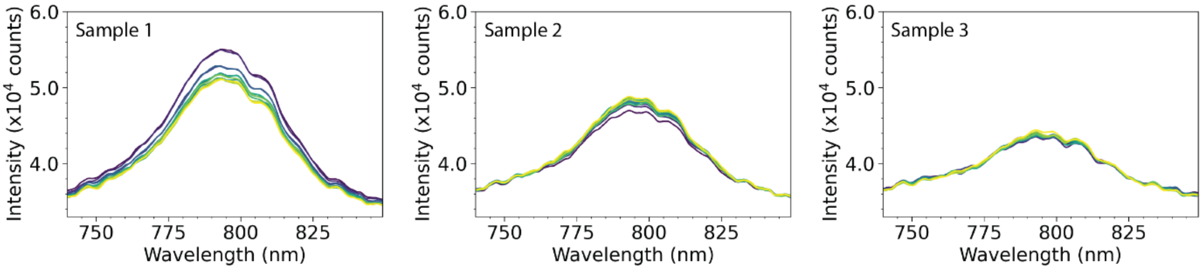

Figure S24. Smoothed PL spectra recorded at a range of magnetic field strengths of three samples per composition. All spectra were recorded using an excitation laser power of 0.3 mW and an integration time of 600 ms, except for the exceptions noted here. (a) Sample 1: 500 ms. (b) Sample 1: 500 ms. (c) Sample 1: 200 ms, sample 3: 500 ms. (d) Sample 1: 500 ms, samples 2 and 3: 0.55 mW.

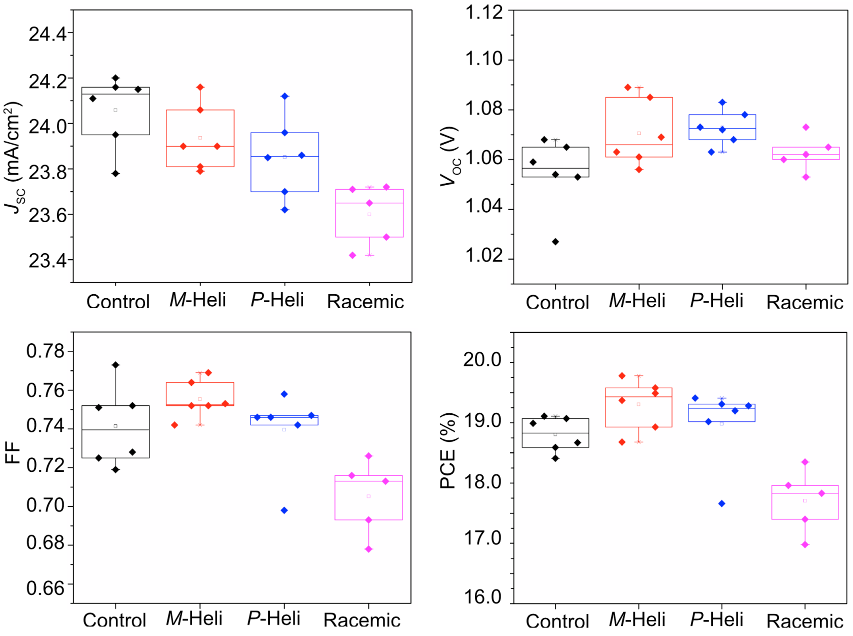

Figure S25. Photovoltaic device performance of alternative compositions. Photovoltaic metrics of control (black) and modulated (color) devices based on $(FA_{0.9}MA_{0.1})_{0.95}Cs_{0.05}Pb_{1.03}I_3$ compositions prepared following *procedure 2*. The racemic mix in the analysis (pink) involves Cl counter-ions, which contribute to further lowering the overall photovoltaic performances (and substantially changing the bandgap, as shown in Figure S15), unlike the I counter ions in the follow-up analysis.

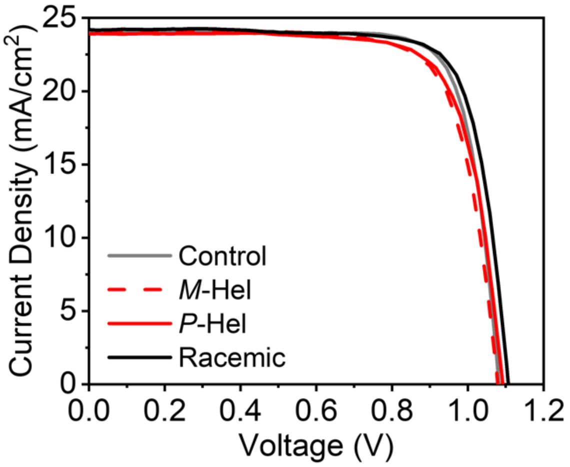

Figure S26. Representative current-voltage characteristics of control (black) and helically modulated (colored) devices based on $FA_{0.97}MA_{0.03}Pb(I_{0.97}Br_{0.03})_3$ compositions prepared following *procedure 1*.

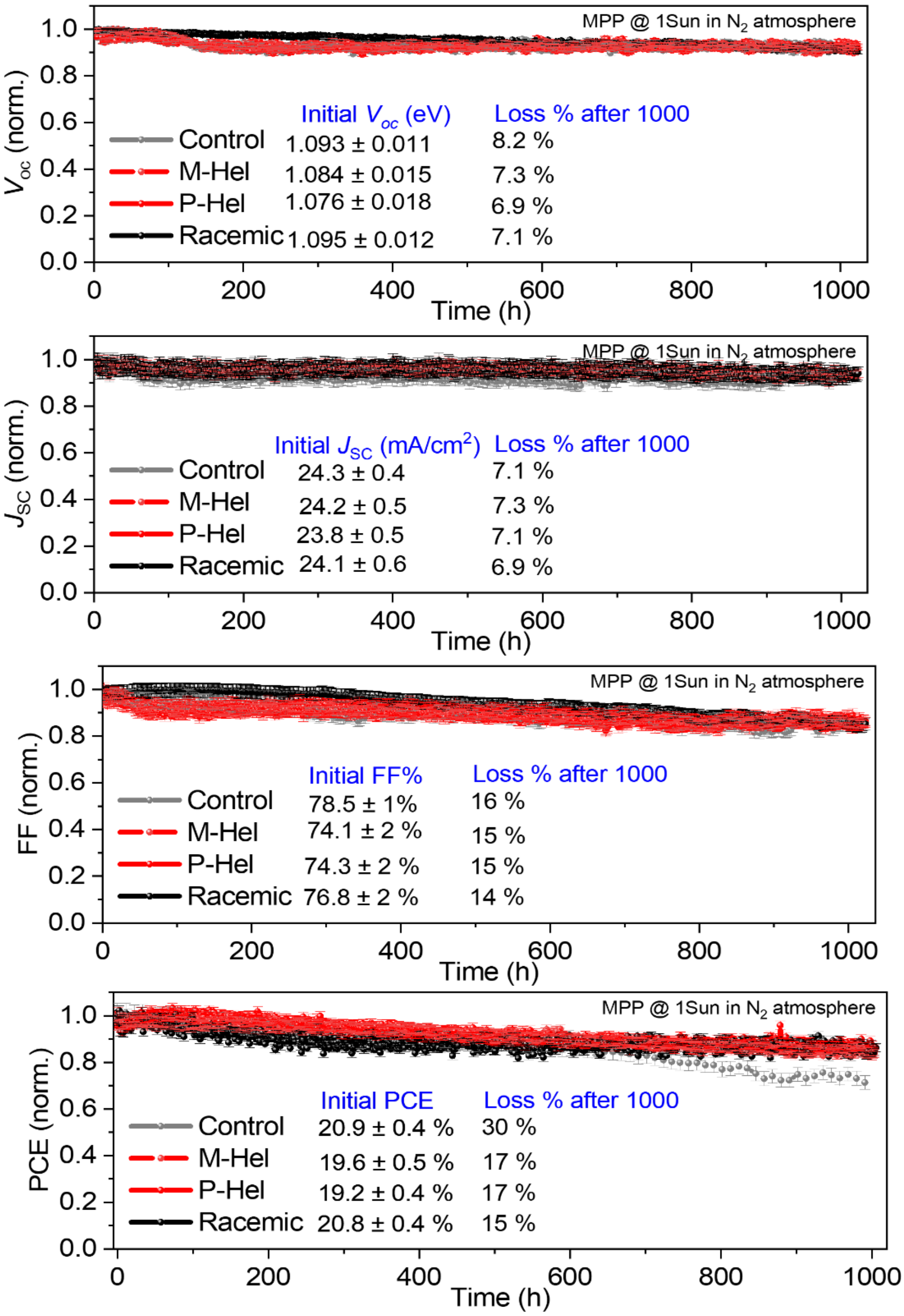

Figure S27. Evolution of photovoltaic performances during operational stability measurements.

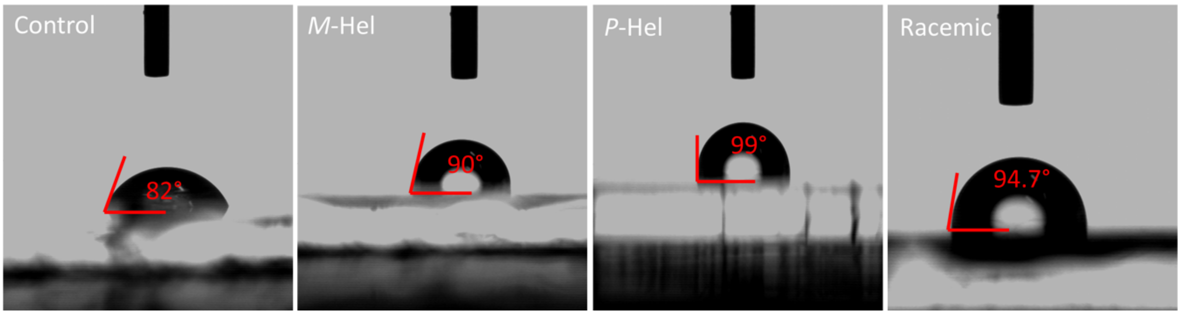

Figure S28. Contact angle measurements of perovskite films with a water droplet.

S3. Supplementary Discussion

The PL spectra of the enantiopure, racemic, and control samples show no significant changes with varying magnetic field strength (Figure S22). To investigate differences smaller than the noise in the data, the spectra were smoothed using Locally Weighted Scatterplot Smoothing (LOWESS), using a smoothing parameter of 0.01. Figure S23 shows good agreement between the raw and smoothed data.

In the smoothed data (Figure S24), some changes in intensity were observed with varying magnetic fields. However, these variations are small and inconsistent over the different samples of the same composition. Therefore, it is likely these variations are not an effect of the magnetic field but could be due to small fluctuations of the excitation laser power or small changes in the alignment caused by the electromagnet heating up during operation. The overall intensity differences between different samples of the same composition might be explained by the manual placement of the sample holder between the poles of the electromagnet, which resulted in a slightly different alignment for every sample. A larger decrease in intensity and a small blue shift with increasing magnetic field strength are observed for one of the M-Heli samples (Figure S23–S24b). Figure S23f shows the same PL spectra of this sample at selected magnetic field strengths (solid), along with PL spectra recorded at those same magnetic field strengths 40 to 100 minutes later than the initial measurements (dashed). The spectra recorded at a later time have a lower intensity and are blue-shifted compared to the spectra recorded earlier at the same magnetic field and show no variation with the magnetic field strength. This indicates that the trend observed in Figure 23d was likely due to degradation and not an effect of the magnetic field. For most other samples, PL spectra in the entire range of magnetic fields were measured within approximately twenty minutes of the 0 mT spectrum, explaining why degradation is not observed for other samples.

In summary, no significant effect of the magnetic field on the PL of the enantiopure or racemic samples was observed. This corresponds well to the independence of the TRPL from a magnetic field (Figure S20), which supports that CISS is not the main effect contributing to the device performance.

References

[1] N. Hellou, C. Jahier-Diallo, O. Baslé, M. Srebro-Hooper, L. Toupet, T. Roisnel, E. Caytan, C. Roussel, N. Vanthuyne, J. Autschbach, M. Mauduit, J. Crassous, *Chem. Commun.* **2016**, *52*, 9243.

[2] N. Hellou, M. Srebro-Hooper, L. Favereau, F. Zinna, E. Caytan, L. Toupet, V. Dorcet, M. Jean, N. Vanthuyne, J. A. G. Williams, L. Di Bari, J. Autschbach, J. Crassous, *Angew. Chem.* **2017**, *129*, 8348.

[3] M. A. Ruiz Preciado, D. J. Kubicki, A. Hofstetter, L. McGovern, M. H. Futscher, A. Ummadisingu, R. Gershoni-Poranne, S. M. Zakeeruddin, B. Ehrler, L. Emsley, J. V. Milić, M. Grätzel, *J. Am. Chem. Soc.* **2020**, *142*, 1645.

[4] T.-S. Su, F. T. Eickemeyer, M. A. Hope, F. Jahanbakhshi, M. Mladenović, J. Li, Z. Zhou, A. Mishra, J.-H. Yum, D. Ren, A. Krishna, O. Ouellette, T.-C. Wei, H. Zhou, H.-H. Huang, M. D. Mensi, K. Sivula, S. M. Zakeeruddin, J. V. Milić, A. Hagfeldt, U. Rothlisberger, L. Emsley, H. Zhang, M. Grätzel, *J. Am. Chem. Soc.* **2020**, *142*, 19980.

[5] T. Kirchartz, J. A. Márquez, M. Stolterfoht, T. Unold, *Adv. Energy Mater.* **2020**, 1904134.